Final Report for the Period ending 6/20/93
Los Alamos National Laboratory Subcontract #9-XC21808D-1
Submitted by A. H. Heuer, Case Western Reserve University

LA-SUB--94-69

Characterization and Evaluation of Y_2O_3-Stabilized Cubic ZrO_2 For Single Crystal Fibers

The goal of this research was to develop the understanding of the structure/property relations in Y_2O_3-stabilized cubic ZrO_2 (Y-CSZ) single crystals with emphasis on the potential use of these materials as a fibrous reinforcement for high temperature structural applications. In particular, the issues addressed include: i) determination of the structure of as-grown Y-CSZ and its relation to the deformation behavior and ii) initial fiber growth and evaluation.

Explanation:

For the contract period ending June 20, 1993, research focused on determination of the structure of as-grown 9.4 mol% Y-CSZ and growth, characterization and evaluation of various cubic ZrO_2 fibers. The body of this report consists of two papers published from this work: 1) High-Strength, Creep-Resistant Y_2O_3-Stabilized Cubic ZrO_2 Single Crystal Fibers and 2) Determination of the Structure of the Cubic Phase in High-ZrO_2 Y_2O_3-ZrO_2 Alloys by CBED. The fiber work was accepted for publication in the *Proceedings of the 17th annual Conference on Composites and Advanced Ceramics:* in press. The structure determination work was accepted for publication in *Phil Mag A:* in press.

DISCLAIMER

HIGH-STRENGTH, CREEP-RESISTANT Y_2O_3-STABILIZED CUBIC ZrO_2 SINGLE CRYSTAL FIBERS

K. J. McClellan, H. Sayir and A. H. Heuer
Department of Materials Science and Engineering
Case Western Reserve University
Cleveland, OH 44106

A. Sayir
NASA-Lewis Research Center
Cleveland, OH 44135

J. S. Haggerty and J. Sigalovsky
Materials Processing Center
Massachusetts Institute of Technology
Cambridge, MA 02139

Y_2O_3-stabilized cubic ZrO_2 (Y-CSZ) single crystal fibers have much higher thermal expansion coefficients than other possible oxide fibers and thus can serve as viable reinforcements for metallic- and intermetallic-matrix composites; furthermore, they offer good isotropic creep resistance. Data is presented for [001] ZrO_2 single crystal fibers (9.5-21 m/o Y_2O_3) grown by the laser heated floating zone process; high temperature strengths were measured as a function of composition and the variation in tensile strength with temperature was measured for 21 m/o Y-CSZ fibers. Strengths of ~2.0 GPa at -196°C, ~1.5 GPa at room temperature and ~500 MPa at 1400°C were achieved. All fibers failed in a brittle manner from surface or near-surface flaws.

INTRODUCTION

Research on potential advanced structural materials has given much emphasis to metallic-, intermetallic-, and ceramic-matrix composites. The goal of extending the use temperature above that which monolithic Ni-base superalloys can withstand requires coating superalloys with thermal barriers or using composites with high melting-point matrices, i.e. refractory metals, intermetallics or ceramics. Furthermore, there is a need for lower temperature applications for such composites if weight savings can be achieved. Ceramic fiber reinforcements for these composites, especially continuous fibers, are a very effective method for retaining

high load carrying capabilities at temperatures where matrix creep can be pronounced.

There are a number of factors that must be considered when choosing a fibrous reinforcement for a composite. A high melting point for the fiber is usually desirable. Related considerations are stability with respect to the matrix and an oxidizing atmosphere, creep resistance, specific stiffness and high temperature strength. Thermal fatigue is also an important issue, and for metallic and intermetallic matrices, a high coefficient of thermal expansion (CTE) has considerable advantage. Sapphire (α-Al_2O_3) fibers have received the most attention as a candidate reinforcement material, and at this time, constitute the benchmark by which other candidate oxide fibers must be judged.

Considerable attention has been focused on intermetallic matrix composites, with much recent effort on the aluminide family (NiAl, Ni_3Al, TiAl, Fe_3Al, etc.). In terms of high melting points and thermodynamic stability, oxide reinforcements are promising fiber candidates. One major drawback, however, is the large mismatch in thermal expansion coefficients between the intermetallics and many oxide ceramics (e.g. sapphire). Table 1 shows that sapphire and YAG, the two most studied oxide fibers, have much lower CTE's than the aluminide family of intermetallics. Y_2O_3 fully-stabilized cubic ZrO_2 (Y-CSZ), on the other hand, has a fairly high CTE and provides a good thermal expansion match with this family of materials (the thermal properties of Y-CSZ, including the composition dependence of the CTE, are discussed elsewhere[1]). This is one of the factors that has sparked the present interest in ZrO_2 as a potential fibrous reinforcement.

Table 1: Thermal expansion coefficients and specific moduli of a number of intermetallics and ceramics

	CTE x10^{-6} /K					10^3 E/ρ GPa/(kg/m^3)
	293 K	500 K	700 K	900 K	1100 K	293 K
NiAl	11.9	13.9	15.2	15.8	16.0	29
Ni_3Al	12.3	13.4	14.3	14.9	15.4	24
TiAl	10.0	11.1	11.4	11.8	12.2	43
Ti_3Al	10.0	-	-	-	-	34
FeAl	17.3	19.3	20.7	21.4	21.7	47
Fe_3Al	8.8	14.3	18.2	24.7	25.0	21
$MoSi_2$	7.4	8.0	8.5	8.9	9.4	70
Al_2O_3	6.8	7.2	7.6	7.9	8.3	97
ZrO_2*	10.7	11.1	11.1	11.7	13.0	41
YAG**	8.5	8.7	8.9	9.0	9.2	68

* 21 m/o Single Crystal Y_2O_3-stabilized ZrO_2

** Single Crystal "white" $Y_3Al_5O_{12}$

Significant research has been done over the years on the high temperature deformation of bulk ZrO_2 alloy single crystals. Y-CSZ demonstrates potent solid solution strengthening,[2] with an increase in solute content from 9.4 to 21 m/o Y_2O_3 resulting in a corresponding ~two-fold increase in flow stress (from 180 to

360 MPa at 1400°C) for the easy glide orientation (Fig. 1). Y_2O_3 partially-stabilized ZrO_2 (Y-PSZ) materials are well known as transformation-toughened ceramics (due to the stress-induced tetragonal to monoclinic transformation) but also exhibit potent high temperature precipitation hardening.[3] This can lead to a further two-fold increase in flow strength to ~700 MPa at 1400°C.[4]

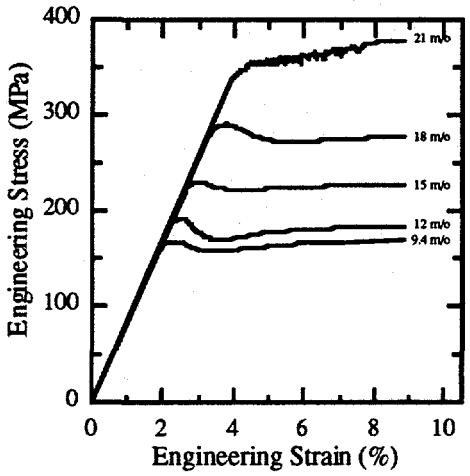

Figure 1. Deformation curves for Y-CSZ alloys with various solute contents. The compression axis was <112>. All tests were performed in air at 1400°C with a strain rate of 1.2×10^{-5} /sec.

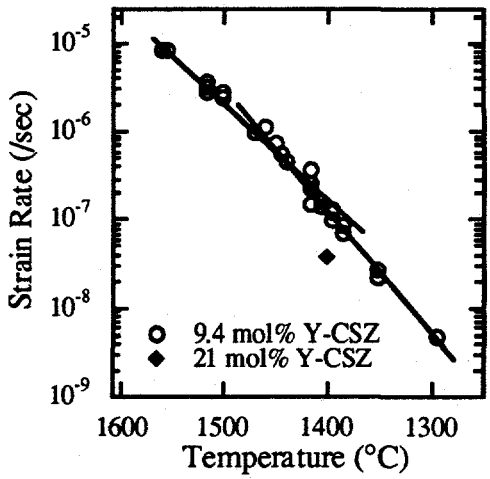

Figure 2. Steady-state creep rate data for compression along <112>, normalized to a stress of 100 MPa. (after Martinez-Fernandez, et al.[5])

At high temperatures a creeping matrix may shed all of its load to the fiber, and both high temperature strength and high temperature creep resistance are essential for fibrous reinforcements. Creep of 9.4 m/o Y-CSZ has been studied;[5,6] the two-fold increase in flow stress at constant strain rate (Fig. 1) in the high solute Y-CSZ translates into a ~fifty-fold increase in creep resistance because of the high stress exponent, as has now been confirmed (Fig. 2) with a single datum at 1400°C (the diamond, whose creep rate is 3.7×10^{-8} /sec at 100 MPa stress), with a further fifty-fold increase possible (and likely) in the precipitation-hardened Y-PSZ alloys.

Corman[6] found that the creep properties of Y-CSZ are fairly isotropic. In contrast, sapphire is strongly anisotropic in its creep resistance and this can be a limiting factor when considering off-axis loading.

EXPERIMENTAL PROCEDURE

Fiber Growth

All fibers were grown at the Materials Processing Center at MIT using a laser float-zone melting technique.[7,8] This crystal growth technique is suitable for ZrO_2, but

is not yet optimized, due to the high melting point (~2750°C) and other thermal properties of Y_2O_3-ZrO_2 alloys. Skull-melted Y-CSZ single crystals* of various compositions were used for feed stock and were oriented using Laue back-reflection x-ray diffraction to provide seed crystals for fiber growth with a <001> orientation. The fiber diameters were progressively reduced during sequential drawing operations to obtain final nominal diameters between ~150 and 220 μm.

Two groups of ZrO_2 single crystal fibers were grown using the laser heated fiber growth process. The first group was grown from ZrO_2 single crystals containing nominally 9.5, 12 and 15 m/o Y_2O_3. For these fibers, the crystals were cut into square cross-section rods having an effective diameter of 0.7-0.8 mm. The feed rods for the second group of ZrO_2 single crystals contained 21 m/o Y_2O_3 and were ground into octagonal cross-section rods with a 0.9 mm effective diameter (the octagonal shape was employed to improve the uniformity of the melting process during growth).

The single crystal fibers were grown in Ar or Ar + 2% O_2 atmospheres at a total pressure of 1 atmosphere. The fiber growth rate was 15 cm/hr from intermediate 400-590 μm diameter fibers; the intermediates were grown at 10 cm/hr from the square or octagonal feed rods.

Thermal analysis of the floating zone process predicts that the temperature gradient at the freezing interface is approximately 8.4×10^3 °C/cm. At a growth rate of 15 cm/hr, the gradient-to-growth rate ratio (G/R) is 2×10^6 °C•sec/cm^2, and the effective cooling rate (G•R product) is 35 °C/sec. The G/R ratio is unusually high, insuring a planar solidification interface; the cooling rate is fast enough to be considered a quench.

Phase contents and compositions of feed rods, intermediates and final fibers for the 15 and 21 m/o Y-CSZ compositions were characterized by powder x-ray diffraction of ground material. Precision lattice cell parameters were calculated from the x-ray patterns using Cu-K_α radiation, with Si as an internal standard, in the 2θ range 25-105° where 9 strong cubic-ZrO_2 peaks are located. Surface features were examined by SEM.

Fiber Testing

The fibers were tested at the NASA-Lewis Research Center using a fast fracture/cold grips testing apparatus.[9] For this testing technique, fibers are epoxied onto index cards which are then aligned and gripped in a screw driven, Instron** mechanical testing machine for tensile testing. All fibers were tested using an 8 mm gage length and a cross-head speed of 1.27 mm/min.

For high temperature testing, fibers were heated with a CO_2 laser, and temperature measurement and control were provided by a two-color optical pyrometer (ModlinePlus™ Infrared Thermometer***). The reliability of the high

---

* CERES Corp., N. Billerica, MA 01862
** Instron Corp., Canton, MA 02021
*** Ircon, Inc., Niles, IL 60648

temperature test capability of this apparatus was confirmed (Table 2) by testing 20 Saphikon* sapphire fibers in this laser furnace and in a conventional high temperature furnace; results were indistinguishable.

Table 2: Statistical comparison of strength data for 20 Saphikon sapphire fibers tested at 1450°C with the Laser Scanning Furnace (LSF) and a conventional Pt-Furnace (Pt-F)

	Tensile Strength (MPa)	
	LSF	Pt-F
Min	641	621
Max	910	834
N	20	20
Mean	710	701
Median	696	692
STD	65	57
Skewness	1.55	0.80

RESULTS AND DISCUSSION

Fiber Growth

Despite the high melting temperatures, CO_2 heating readily forms stable ZrO_2 melts of all the compositions investigated from which fibers can be pulled. However, Y-CSZ does present some unusual issues with respect to producing high quality fibers under stable conditions.

The melt volumes, and consequently the diameters of the growing fibers, are not as stable as is observed with other oxides, e.g. sapphire; these variations result from two factors. For the lower Y_2O_3 concentrations, the fibers tended to be black unless the zone lengths were minimized, thereby minimizing the superheat and the propensity to cause thermal reduction. Even with minimum zone lengths, however, the optical properties varied along the fiber lengths, causing the radiant heat flux through the fibers to vary in a manner that influenced the zone volume. With one exception (which was black, i.e. reduced ZrO_2), the 21 m/o Y_2O_3 fibers were colorless and transparent even when grown with longer melt zones. The second factor, which affected diameter fluctuations, resulted directly from the very low thermal conductivity of ZrO_2. The corners on the square feed rods did not melt uniformly, which caused relatively large variations in the diameters of the resulting crystals. The octagonal feed rods used exclusively for the 21 m/o Y_2O_3 fibers reduced this problem.

The 21 m/o Y_2O_3 fibers were circular in cross-section and diameters were generally as uniform and smooth as have been achieved with single crystal fibers of other materials. The diameters of fibers grown in the first group (with lower Y_2O_3 concentrations) exhibited much greater variations in diameters for the cited reasons; however, their cross-sections were roughly circular and their surfaces were smooth on a microscopic scale. None of the ZrO_2 fibers exhibited the propensity to facet

---

* Saphikon, Inc., Milford, NH 03055

strongly during steady state growth that is exhibited by [111] spinel[10] or a-axis sapphire.[11] Pronounced facets were evident only when the fiber diameters changed rapidly either during expansion from the seed or during termination. These special facets have 4-fold symmetry about the [001] fiber growth axis. However, modest faceting usually occurs and is implicated in the fracture (see below).

Both optical and SEM micrographs of 21 m/o Y_2O_3 fibers showed two very closely spaced linear features (wavelength 1-3 μm and ~10 μm) on the fiber surfaces oriented perpendicular to the [001] growth axes. In steady state sections of the fibers, they are extremely difficult to image and there is no clear evidence that the linear features result from faceting. The fibers were grown at a rate of 41 μm/s, so these features must have formed at rates ranging from 4 to 40 Hz. Observations, with fast optical detectors, of light emitted from the molten zone revealed no fluctuations in emitted light in this frequency range. Although the features are small in size, fractography (see below) showed many instances where the surface features correlated with the fine (~1 μm) steps on the fracture surfaces. No critical flaws were associated with the diametrical fluctuations.

X-ray analysis of feed, intermediate and fiber samples of the 21 m/o alloy showed that all three contained only cubic ZrO_2. Thirty-five lattice parameters measured by Ingel and Lewis[12] for different concentrations of Y_2O_3 in cubic ZrO_2-Y_2O_3 solid solutions were fitted with a linear regression analysis to give a(nm) = 0.51168 + 0.000258•m/o Y_2O_3. The Y_2O_3 concentrations in the three sample types are given in Table 3.

Table 3: Lattice parameter data for Y-CSZ fiber growth

Sample	a (nm)	Y_2O_3 (m/o)
Feed	0.51723±0.00003	21.5±0.1
Intermediate	0.51695±0.00010	20.4±0.4
Final Fiber	0.51736±0.00002	22.0±0.1

The indicated error in Y_2O_3 content corresponds only to the statistical error attributed to the lattice parameter calculations. Taking into account the significant scatter of the reference data about the best fit line (at least ±0.5 m/o), the lattice parameters of all three sample types should be considered equal to each other and to the nominal 21 m/o Y_2O_3 concentration. This indicates that there was no preferential loss of Y_2O_3 or ZrO_2 from the melts.

Mechanical Testing

Two sets of fibers have been grown and tested to date. The first set consisted of fibers of several solute contents (9.5, 12 and 15 m/o Y_2O_3) tested in air at 1400°C. The results of this series of tests, Table 4, indicates high temperature strengths greater than 450 MPa in all cases, but the scatter in the data is such that no compositional effect on strength, or a lack thereof, can be determined. A survey of the apparent fiber quality using optical microscopy shows significant variability in the fiber diameter, a clear manifestation of the difficult growth condition and the developmental nature of the first set of ZrO_2 growth runs. Fractography was performed on the fibers; for this strain rate failure occurred by brittle fracture in all

Table 4: Developmental-fiber data for first growth fibers tested in air at 1400°C

Fiber Composition [m/o Y_2O_3]	Mean Strength [MPa]	Standard Deviation [MPa]	Number of Fibers Tested
9.5	454	45	8
12	463	115	10
15	522	31	2
21*	497	62	5

* Data from second fiber growth

cases, which was invariably nucleated by surface or near-surface flaws. The second batch of fibers was grown from 21 m/o Y-CSZ feed stock, inasmuch as this alloy composition exhibited the maximum in solid solution strengthening (Fig. 1). Again, there were some fluctuations in fiber diameter along the gage length. This batch of fibers was tested at -196°C, room temperature, 950-1000°C, 1200°C, 1400°C and 1470°C. The low temperature and high temperature data are shown in Fig. 3a and 3b, respectively. The low temperature strengths (median strength at -196°C, 2.01 GPa; median strength at room temperature, 1.52 GPa) are impressive and demonstrate that classical stress corrosion can also occur in this system. Using various assumed flaw geometries (from an edge-notch to a full-circular score) with a brittle fracture strength of 2.0 GPa and a K_{IC} of 1.1 MPa•$m^{1/2}$,[13] the size of the critical flaws appears to be in the submicron range.

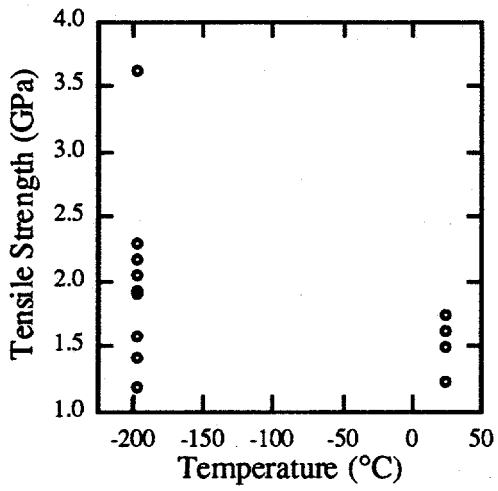

Figure 3a. Strength data for 21 m/o fibers tested at liquid nitrogen (median of 2.01 GPa) and room temperature (median of 1.52 GPa).

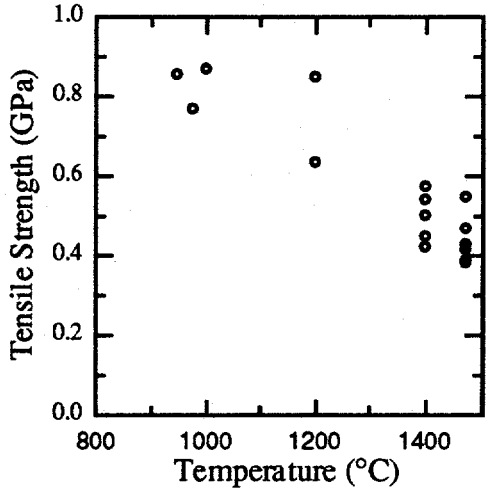

Figure 3b. Strength data for 21 m/o fibers showing that at high temperatures strength is fairly temperature-independent.

The high temperature strengths, a median value of 568 MPa, are equally impressive and suggests that in this temperature range, the strength is not a function of temperature. Of even more significance, the strength reduction between room temperature and high temperatures is much less than for sapphire fibers.[14] Thus, improvement in fiber quality through growth optimization should translate into further improvements in high temperature strengths.

Fractography of the 21 m/o Y-CSZ fibers showed that all fibers fractured in a brittle manner from surface or near-surface flaws, even those tested at high temperatures (Fig. 4a); in essentially all cases, a facet is implicated in the fracture. Steps on the fiber surface within the hot-zone appear to be a manifestation of thermal etching and are exaggerated on the fiber facets (Fig. 4b).

Figure 4a. SEM micrograph showing a fracture surface from a 21 m/o Y_2O_3 fiber that was tested at 1200°C and had a strength of 868 MPa.

Figure 4b. Apparent thermal etching is evident from surface steps perpendicular to the fiber axis; the tendency for surface steps to be enhanced on fiber facets is apparent.

CONCLUSIONS

High thermal expansion creep resistant Y_2O_3-stabilized cubic ZrO_2 fibers have been grown by laser float-zone melting and have been tested between -196°C and 1470°C. At all temperatures, the strengths are impressive and are limited by surface defects associated with the yet-to-be optimized crystal growth; at the low temperatures, -196°C, the highest strength achieved was 3.6 GPa while the median strength was 2.0 GPa. The difference in strength between -196°C and room temperature suggests classic stress corrosion. The strength at high temperature, 950°C - 1470°C, is temperature-independent and ~ 0.5 GPa; brittle fracture is still observed. The high temperature strength represents a very high fraction of the low temperature strength, especially compared to competing oxide fibers such as sapphire.

ACKNOWLEDGMENTS

The authors would like to thank CERES Corp. for generously donating the feed stock material for the fiber growth. and support from Los Alamos National Laboratory.

REFERENCES

[1] K. J. McClellan and A. H. Heuer, "Thermal Expansion Measurements for High Solute Y-CSZ Alloys from Room Temperature to 1400°C," to be published

[2] A. Dominguez-Rodriguez, A. H. Heuer and J. Castaing, "Dislocations and the Mechanical Properties of Stabilized ZrO_2, "*Rad. Effect. and Def. in Sol.*, **119-121**, 759-769 (1991)

[3] A. Dominguez-Rodriguez, V. Lanteri and A. H. Heuer, "High-Temperature Precipitation Hardening of Two-Phase Y_2O_3-Partially-Stabilized ZrO_2 Single Crystals: A First Report," *J. Am. Ceram. Soc.*, **69**[3] 285-287 (1986)

[4] J. Martinez-Fernandez, M. Jimenez-Melendo, A. Dominguez-Rodriguez, P. Cordier and A. H. Heuer, "Precipitation Hardening in <001> Oriented Y-PSZ Single Crystals," to be published

[5] J. Martinez-Fernandez, M. Jimenez-Melendo, A. Dominguez-Rodriguez and A. H. Heuer, "High-Temperature Creep of Yttria-Stabilized Zirconia Single Crystals," *J. Am. Ceram. Soc.*, **73**[8] 2452-56 (1990)

[6] G. S. Corman, "High-Temperature Creep of Some Single Crystal Oxides," *Ceram. Eng. Sci. Proc.*, **12**[9-10] 1745-1766 (1991)

[7] J. S. Haggerty and W. P. Menashi, "Production of Oxide Fibers by a Floating Zone Fiber Drawing Technique," NASA, Contract No. NAS3-13479, Feb. 1971

[8] J. S. Haggerty, W. P. Menashi and J. F. Wenckus, Method for Forming Refractory Fibers by Laser Energy, USP 3,944,640, Mar. 16, 1976

[9] W. Penn, "Innovative Fiber Laser Furnace," NASA, Contract No. NAS3-26133, Oct. 1991

[10] J. Sigalovsky, K. C. Wills, J. S. Haggerty and J. E. Sheehan, "Growth, Characteristics and Properties of Spinel Single Crystal Fibers," *Ceram. Eng. Sci. Proc.*, **13**[7-8] 183-189 (1992)

[11] J. S. Haggerty, K. C. Wills and J. E. Sheehan, "Growth and Properties of Single Crystal Oxide Fibers," *Ceram. Eng. Sci. Proc.*, **12**[9-10] 1785-1801 (1991)

[12] R. P. Ingel and D. Lewis III, Lattice Parameters and Density for Y_2O_3-Stabilized ZrO_2, *J. Am. Ceram. Soc.*, **69**[4] 325-32 (1986)

[13] G. N. Morscher, P. Pirouz and A. H. Heuer, "Temperature Dependence of Hardness in Yttria-Stabilized Zirconia Single Crystals," *J. Am. Ceram. Soc.*, **74**[3] 491-500 (1991)

[14] J. A. Dicarlo, G. B. Hurst, G. Morscher, G. Selover and A. Sayir, "Current Issues for SiC and Oxide Fiber Development," HITEMP Review. Advanced High Temperature Engine Materials Technology Program, *Proc. 2nd Ann HITEMP Review*, **50**, 1-12 (1990)

Determination of the Structure of the Cubic Phase in high-ZrO_2 Y_2O_3-ZrO_2 Alloys by CBED

K. J. McClellan, S.-Q. Xiao, K. P. D. Lagerlof and A. H. Heuer
Department of Materials Science and Engineering
Case Western Reserve University
Cleveland, OH 44106

ABSTRACT

Convergent beam electron diffraction (CBED) was used to determine the space group of 9.9 and 18 mol% Y_2O_3-stabilized cubic ZrO_2 (Y-CSZ) single crystals. The result ($P\bar{4}3m$ space group) is different from the known tetragonal structure ($P4_2/nmc$ space group) present in lower solute (3.2 mol% Y_2O_3) alloys, and the cubic structure (space group $Fm\bar{3}m$) traditionally assumed for cubic ZrO_2. The oxygen sublattice of the cubic structure is distorted from $Fm\bar{3}m$, relative to the cation sublattice, by displacements along the <111> directions. Computer simulations of the CBED patterns agree with experiment and suggest an anion displacement of ~0.3 Å from the {1/4,1/4,1/4} positions of the ideal fluorite structure.

I. INTRODUCTION

Pure ZrO_2 has cubic (*c*) symmetry at temperatures above 2370°C, tetragonal (*t*) symmetry from 1170°C to 2370°C and monoclinic (*m*) symmetry below 1170°C (Stubican and Hellmann 1981). The cubic and tetragonal structures can be retained at room temperature by alloying with various oxide "stabilizers", e.g. Y_2O_3, MgO, CaO or CeO_2. The dopant cation substitutes for Zr on the cation sublattice and if aliovalent, causes formation of charge compensating oxygen vacancies. In such doped crystals, these oxygen vacancies and the accompanying lattice relaxation are thought to permit the metastable retention of the *c* or *t* phase to room temperature (Morinaga, Adachi and Tsukada 1983, Osborn *et al.* 1986). In the Y_2O_3-ZrO_2 system, lattice parameter and diffraction studies

(Steele and Fender 1974, Scott 1975, Zhou, Lei and Sakuma 1991) suggest that $\geq$8 mol% Y_2O_3 is needed to retain cubic symmetry to room temperature; we refer to such materials as Y-CSZ for Y_2O_3 -stabilized cubic ZrO_2.

The monoclinic structure has been determined by McCullough and Trueblood (1959) and belongs to the $P2_1/c$ space group, while Teufer (1962) determined the space group of the tetragonal phase to be $P4_2/nmc$; these structures have typically been described in terms of a distortion from the ideal fluorite structure with the $Fm\bar{3}m$ space group, which has usually been assumed for *c*-ZrO_2. However, several studies (Carter and Roth 1968, Steele and Fender 1974, Faber, Mueller and Cooper 1978, Morinaga, Cohen and Faber 1979, Horiuchi, Schultz, Leung and Williams 1984, Catlow, Chadwick, Greaves and Moroney 1986, Howard, Hill and Reichert 1988, Howard and Hill, 1991; Zhou *et al.* 1991) have revealed {odd,odd,even} reflections in Y-CSZ, which are forbidden for the $Fm\bar{3}m$ space group in which the Zr atoms occupy the 1(a) (000) positions and the O atoms occupy the 8(c) {1/4,1/4,1/4} positions. Structure refinements based on these neutron or x-ray scattering studies indicate that the O atoms are displaced (up to 0.5Å) from the ideal {1/4,1/4,1/4} fluorite positions along either <100> or <111>.

It is important to note that the diffraction symmetry of a crystal may not be identical to the crystal symmetry; the space group of a perfect crystal may be related to but not equivalent with the structure determined from consideration of the diffraction symmetry. For instance, once the O atoms undergo any displacement from the {1/4,1/4,1/4} fluorite positions, they would occupy more general sites, e.g. 32(f) in the $Fm\bar{3}m$ space group. Thus, if an O atom occupies an (x,x,x) position, the $Fm\bar{3}m$ symmetry operations generate another 31 equivalent O atoms within a unit cell. However, in order to maintain the Zr:O ratio of 1:2, only eight oxygen atoms are allowed within a unit cell containing four ZrO_2 "molecules" (neglecting the oxygen vacancies introduced by Y substitution). This situation would violate the space group principle, i.e. a perfect unit cell must exhibit the complete

symmetry of the space group and the structure of c-ZrO_2 must belong to a space group other than $Fm\bar{3}m$. The experimental data indicate that this space group should still be cubic but must be primitive to give rise to the observed {odd,odd,even} and {111} type reflections; the {odd,odd,even} reflections, in particular, cannot be explained as tetragonally-distorted regions within a $Fm\bar{3}m$ cubic matrix, or using fractional occupancy within the $Fm\bar{3}m$ structure, as these assumptions violate the space group principle.

Consider the structure factor, F_{hkl}, for the hkl reflection for x-ray or electron diffraction

$$F_{hkl} = \sum_{1}^{N} f_n e^{2\pi i(hu_n + kv_n + lw_n)} \qquad (1)$$

where f_n is the atomic scattering factor for the n^{th} atom and N is the total number of atoms in the unit cell. As is well known, c-ZrO_2 with the ideal fluorite structure would have Zr at 0,0,0 + fcc translations and O at 1/4,1/4,1/4 and 1/4,1/4,3/4 + fcc translations, so that equation 1 becomes

$$\begin{aligned} F_{hkl} &= f_{Zr}e^{2\pi i(0)} + f_{Zr}e^{2\pi i(\frac{1}{2}+\frac{1}{2})} + f_{Zr}e^{2\pi i(\frac{1}{2}+\frac{1}{2})} + f_{Zr}e^{2\pi i(\frac{1}{2}+\frac{1}{2})} \\ &\quad + f_O e^{2\pi i(\frac{1}{4}+\frac{1}{4}+\frac{1}{4})} + f_O e^{2\pi i(\frac{1}{4}+\frac{1}{4}+\frac{3}{4})} + f_O e^{2\pi i(\frac{1}{4}+\frac{3}{4}+\frac{1}{4})} + f_O e^{2\pi i(\frac{3}{4}+\frac{1}{4}+\frac{1}{4})} \\ &\quad + f_O e^{2\pi i(\frac{1}{4}+\frac{3}{4}+\frac{3}{4})} + f_O e^{2\pi i(\frac{3}{4}+\frac{1}{4}+\frac{3}{4})} + f_O e^{2\pi i(\frac{3}{4}+\frac{3}{4}+\frac{1}{4})} + f_O e^{2\pi i(\frac{3}{4}+\frac{3}{4}+\frac{3}{4})} \\ &= f_{Zr}[1 + e^{\pi i(h+k)} + e^{\pi i(h+l)} + e^{\pi i(k+l)}] + f_O e^{\frac{\pi i}{2}(h+k+l)}[1 + e^{\pi il} + e^{\pi ik} + e^{\pi ih} \\ &\quad + e^{\pi i(k+l)} + e^{\pi i(h+l)} + e^{\pi i(h+k)} + e^{\pi i(h+k+l)}] \end{aligned} \qquad (1a)$$

so that

$$F_{Zr} = \begin{bmatrix} 4 \\ 0 \end{bmatrix} f_{Zr} \quad \begin{matrix} \text{unmixed indices} \\ \text{mixed indices} \end{matrix}$$

$$F_O = \begin{bmatrix} 8 \\ 0 \end{bmatrix} f_O \quad \begin{matrix} \text{all even indices} \\ \text{any odd indices} \end{matrix},$$

and the structure factor for c-ZrO_2 can be written

$$F_{hkl} = \begin{bmatrix} 4f_{Zr} + 8f_O \\ 4f_{Zr} \\ 0 \end{bmatrix} \quad \begin{matrix} \text{all - even indices} \\ \text{all - odd indices} \\ \text{mixed indices} \end{matrix}.$$

Clearly, mixed index reflections are forbidden, and reflections with all-odd indices will be relatively weak. If the oxygen atoms are displaced by $\{\delta_u, \delta_v, \delta_w\}$ from the ideal fluorite structure positions, equation 1a becomes

$$\begin{aligned} F_{hkl} = {} & f_{Zr}[1+e^{\pi i(h+k)}+e^{\pi i(h+l)}+e^{\pi i(k+l)}] \\ & + f_O e^{\frac{\pi}{2}(h+k+l)} e^{2\pi i(\delta_u h+\delta_v k+\delta_w l)}[1+e^{\pi il}e^{-4\pi i\delta_w l}+e^{\pi ik}e^{-4\pi i\delta_v k} \\ & + e^{\pi ih}e^{-4\pi i\delta_u h}+e^{\pi i(k+l)}e^{-4\pi i(\delta_v k+\delta_w l)}+e^{\pi i(h+l)}e^{-4\pi i(\delta_u h+\delta_w l)} \\ & + e^{\pi i(h+k)}e^{-4\pi i(\delta_u h+\delta_v k)}+e^{\pi i(h+k+l)}e^{-4\pi i(\delta_u h+\delta_v k+\delta_w l)}]. \end{aligned} \quad (1b)$$

Because the δ's are not integer, the structure factor is non-zero for mixed reflections. If the displacements are along the cube diagonals, cubic symmetry will be retained, but if the displacements are along a single cube axis, i.e. $\delta_u = \delta_v = 0$, the symmetry will be tetragonal (but three tetragonal variants might be expected).

Convergent beam electron diffraction (CBED) is a very powerful technique for crystal point group and space group determination (Tanaka 1989), and in this work, was performed on 9.9 and 18 mol% Y-CSZ materials and on a 3.2 mol% alloy with *t* symmetry for reference. The diffraction information from the 9.9 mol% alloy violated $Fm\bar{3}m$ symmetry and was not consistent with the known tetragonal structure ($P4_2/nmc$) of the 3.2 mol% alloy. Analysis of the CBED structure allowed the correct structure of *c*-ZrO_2 to be determined; the space group is in fact $P\bar{4}3m$. Displacements on the oxygen sublattice will be discussed in light of the newly-determined crystal structure.

II. EXPERIMENTAL PROCEDURE

TEM thin foils were prepared in a conventional manner for three alloys containing 3.2* , 9.9** and 18** mol% Y_2O_3, the later two in single crystal form. After conventional Ar ion thinning to perforation, the thin foils were further milled at 3keV and 1mA with a

---

* Y-TZP, Coors Ceramics Co., Golden, CO, 80401

** Skull-melt grown single crystals, CERES Corp., N. Billerica, MA, 01862

beam incidence angle of ~12° for 20 minutes to minimize surface damage and contamination; a minimal layer of carbon was then applied to prevent charging. CBED analysis was performed at 120keV with a typical probe size of ~40nm;*** use of a cold stage at ~160°C did not substantially improve the CBED patterns.

Computer simulation of CBED patterns utilized the Bloch wave method with the Electron Microscopy Software (EMS) package (Stadelmann 1987) for generating two-dimensional zero order Laue zone (2-D ZOLZ) patterns; particular focus was given to the effect of oxygen displacements from $Fm\bar{3}m$ symmetry and thickness variations on CBED patterns.

III. RESULTS

3.1 SAD Patterns

Selected area diffraction (SAD) patterns of the <111>, <110>, and <100> zone axes from the 9.9 mol% crystal are shown in Fig. 1; they suggest a fcc lattice with the exception of the "forbidden" {odd, odd, even} reflections. The symmetry of these patterns is identical with those of the 18 mol% crystal, except that the "forbidden" reflections were missing for the higher solute crystal.

3.2 CBED Analysis

Various ZOLZ zone axis CBED patterns will be presented for the three alloys; for convenience, however, the bright field (BF) and whole pattern (WP) symmetries observed in the various zone axes for each sample are summarized in Table 1. (The HOLZ line information in the BF disks is uncertain in these alloys because the large concentration of charge-compensating oxygen vacancies reduces the HOLZ line intensities and correspondingly increases the background intensity.)

*** Philips CM20 AEM, Mahwah, NJ, 07430

3.2.1 <111> Zone Axis Pattern

The <111> zone axis patterns for the 3.2 and 9.9 mol% alloys in Figs. 2a and 2b confirms the tetragonal (cubic) symmetry of the 3.2 (9.9) mol% alloy as it shows the expected m (3m) symmetry, although the differences between the two patterns are subtle. (While HOLZ lines are a sensitive indicator of unit cell distortions (Randle, Barker and Ralph 1989), the weakness or absence of HOLZ lines within the BF disc and the small atomic displacements in these crystals (see below) suggests that the two-dimensional information in the ZOLZ patterns may be the most useful indicator of symmetry in defective crystals.) At first glance (Fig. 2c), the 18 mol% alloy pattern shows 6mm symmetry, but this high symmetry is largely an artifact caused by the high point defect concentration; a CBED pattern taken with a small camera length (Fig. 2d) clearly shows 3m symmetry.

Figs. 1 and 2 show that the 9.9 mol% alloy has cubic rather than tetragonal symmetry (the possibility that the 3-fold symmetry results from averaging of all tetragonal variants can be excluded and will be discussed below). There are 5 possible cubic point groups, and using the CBED pattern symmetry tables of Buxton, Eades, Steeds and Rackman (1976) (summarized in Table 2), only $m\bar{3}m$ and $\bar{4}3m$ show 3m WP symmetry along <111>. Using a <111> zone axis orientation, it is possible to differentiate between these point groups by several methods, e.g. **+g/-g** excitation (Buxton *et al.* 1976) or symmetrical many beam patterns (Tanaka, Saito and Sekii 1983), but study of other high symmetry zone axes is more useful here.

3.2.2 <100> and <110> Zone Axis Patterns

The <100> zone axis CBED pattern (Fig. 3) for the 9.9 mol% sample shows 4mm BF and WP symmetries, while the <110> zone axis WP pattern (Fig. 4) has only a single mirror plane. Thus, the results in Figs. 3 and 4 are superficially contradictory, in that the CBED analysis for the <100> zone axis indicates $m\bar{3}m$ point symmetry, while that for the <110> zone axis indicates $\bar{4}3m$ point symmetry. Inasmuch as small displacements on only

one sublattice are expected, we place more confidence in the clear loss of the second mirror for the <110> zone axis, and suggest that this material belongs to the $\bar{4}$3m point group.

It should be noted that regions which generate relatively strong {odd,odd,even} reflections in conventional SAD patterns most clearly showed m symmetry in <110> zone axis patterns, while other regions exhibited an apparent 2mm WP symmetry; this may be associated with point defect (compositional) inhomogeneities. However, the loss of symmetry was observed in various regions and thicknesses. In view of the apparent discrepancy mentioned above and the variable evidence for $\bar{4}$3m symmetry, it is important to examine the <110> WP data more closely.

The ZOLZ WP for the 9.9 mol% alloy clearly shows a single mirror normal to <01$\bar{1}$> when using an incident probe size of 20-100nm. The transmitted disc has m symmetry rather than the 2mm symmetry predicted in Table 2 for the $\bar{4}$3m BF symmetry. However, for determination of the BF symmetry from dynamical contrast within the 000 disc, the patterns must be recorded under Kossel-Möllenstedt conditions, i.e. non-overlapping discs must be present in the pattern. The ZOLZ pattern in Fig. 4 has significant overlap of the 000 and *hkl* discs, i.e. Kossel pattern conditions are satisfied, and the symmetry observed in the 000 disc is due to beam interaction; BF symmetry is not defined for a Kossel pattern. Reduction of the convergence angle by introducing a smaller C_2 aperture produces a Kossel-Möllenstedt pattern (Fig. 4b), in which the expected BF (2mm) and WP (m) symmetries of the $\bar{4}$3m point group are observed. This change in apparent symmetry is also confirmed by computer simulations (Fig. 5).

Because displacements are only expected on the oxygen sublattice and because of the defect-rich nature of these alloys, it is not possible to determine the space group by examination of lines of dynamic extinction (Tanaka, Sekii and Nagasawa 1983). Hence, it is necessary to consider the reflections present in the SADPs (Fig. 1) to determine the space group. There are six possible space groups with the $\bar{4}$3m point symmetry: P$\bar{4}$3m, P$\bar{4}$3n,

$I\bar{4}3m$, $I\bar{4}3d$, $F\bar{4}3m$ and $F\bar{4}3c$, and the presence of {112}, {110} and {111} reflections eliminate all face-centered (F) and body-centered (I) space groups, so that only $P\bar{4}3m$ and $P\bar{4}3n$ remain. {111} reflections are forbidden for $P\bar{4}3n$ so the 9.9 mol% alloy must belong to the $P\bar{4}3m$ space group.

The <110> ZOLZ pattern for the 18 mol% alloy exhibits symmetry very close to the 2mm BF and WP symmetry of the $m\bar{3}m$ point group (Fig. 6), but a perfect 2mm WP symmetry was not observed. The foil showed the single m symmetry of $\bar{4}3m$ to varying extents; however, the symmetry reduction from 2mm is never as apparent as for the 9.9 mol% crystal. This suggests that even this high solute alloy may not belong to the $Fm\bar{3}m$ space group but rather belongs to $P\bar{4}3m$, with the oxygen sublattice being *on average* only slightly distorted from the 1/4,1/4,1/4 fluorite positions (see below).

In keeping with the previous models of the ZrO_2 structures, we shift the oxygen atoms relative to a stationary cation sublattice along the cube diagonal to retain the cubic $\bar{4}3m$ symmetry. The available sites for $P\bar{4}3m$ suggests that the cations occupy the 1(*a*) and 3(*c*) face centered cubic sites, while the anions occupy two sets of the 4(*e*) sites (Table 3); the anion positions would be {1/4-δ,1/4-δ,1/4-δ} and {3/4-γ, 3/4-γ,3/4-γ} , with $\delta=\gamma$. In a manner analogous to that of *t*-ZrO_2, the first set of oxygens is displaced toward the cell corners while the second set is displaced towards the center of the unit cell (Fig. 7). Displacing all eight anions in the same sense would result in a $Pm\bar{3}m$ space group, contrary to the CBED data. However, the strong relationship between the $P\bar{4}3m$, $Pm\bar{3}m$, and $Fm\bar{3}m$ space groups should be noted. $Pm\bar{3}m$ is a translationengleiche (Type I) non-isomorphic supergroup of $P\bar{4}3m$ and a klassengleiche (Type II) minimal non-isomorphic supergroup of $Fm\bar{3}m$. Thus, in our model for the $P\bar{4}3m$ cubic structure, if $\delta=\gamma=0$ then the $Fm\bar{3}m$ fluorite structure is produced. As will now be shown, the $P\bar{4}3m$ structure allows the distorted fluorite structure to be described without invoking fractional occupation.

The $P\bar{4}3m$ structure was used to simulate 2-D ZOLZ CBED patterns (Fig. 8) for the <111>, <100> and <110> zone axes. The symmetry of these patterns agree well with experiment -- for instance, the <110> 2-D ZOLZ pattern demonstrates only a single mirror perpendicular to $<01\bar{1}>$. By varying the oxygen displacements such that a reduction of symmetry to a single mirror for the <110> zone axis is visible but the apparent symmetry of the <100> zone axis is still 4mm; we estimate δ to be ~0.3Å. <111> oxygen displacements have also been observed in x-ray and neutron scattering experiments (Appendix), which range up to 0.5Å (Morinaga *et al.* 1979).

Simple ordering on the cation sublattice may also be possible in these alloys. Structure factor calculations and CBED simulations indicate that such ordering is consistant with $P\bar{4}3m$ but not $Fm\bar{3}m$ symmetry. However, scattering factors for Y and Zr are so similar for x-ray diffraction that cation ordering alone cannot account the deviation from $Fm\bar{3}m$ symmetry that has been observed. Furthermore, cation ordering alone cannot account for the present CBED results and any accompanying anion displacements must be along <111> to retain the $P\bar{4}3m$ symmetry that has been determined.

As noted earlier, regions exhibiting apparent $m\bar{3}m$ (2mm pattern) symmetry are often observed. The loss of the mirror whose normal is parallel to <002> is less pronounced than might be expected from the proposed $P\bar{4}3m$ structure due to short-range order and/or point defects. Zhou *et al.* (1991) noted a reduction in domain size in the so-called *t'*-ZrO_2 with increasing solute content, and microdomains have been proposed for Ca- and Y-CSZ (Morinaga *et al.* 1980) with a spatial extent ≤30Å. Inherent to the proposed $P\bar{4}3m$ structure is the possibility of two variants of the structure which are related by a 180° rotation about <110> (Fig. 9), i.e. there are two sets of 4 oxygens which have been confined to equivalent <111> displacements of opposite sense from the ideal fluorite positions. Assuming a random distribution of microdomains of the two variants and a probe interaction volume greater than the microdomain size, the <110> CBED pattern

would tend to an *average* 2mm symmetry. This notion is supported by the experimental observation that the single m symmetry becomes more prominent as the probe size is reduced or a thinner region is examined. A second factor which might suggest an apparent 2mm pattern symmetry is the large concentration of isolated point defects and consequent defect ordering (Osborn *et al.* 1986).

IV. DISCUSSION

CBED analysis of the 9.9 and 18 mol% crystals suggests that these Y-CSZ alloys belong to the $\bar{4}3m$ point group and that the structure is that shown in Fig. 7. However, it might be argued that i) a new tetragonal phase is present, the interaction volume of the CBED probe being sufficiently large that all *t* variants are sampled and an "averaged" cubic symmetry is observed, or ii) that regions with tetragonal distortions are present within an $Fm\bar{3}m$ matrix, the probe interaction volume again being sufficiently large that all *t* variants in the two-phase material are sampled.

The first case (analogous to arguments put forward by Zhou *et al.* 1991) requires a tetragonal structure with an axiality of unity; the oxygen sublattice shows distortions of the type {1/4+δ,1/4,1/4} for all variants. This structure could be expected to yield the 3m and 4mm symmetries observed in the <111> and <100> zone axes. However, all zone axis patterns would show the averaged symmetry and so the <110> zone axis would exhibit 2mm symmetry rather than the single mirror (m) symmetry observed in the regions that generated the {odd,odd,even} reflections. Furthermore, such a structure might produce some anti-phase domain boundaries (APBs) at the intersection of two *t* variants, which were not observed using high resolution electron microscopy. The second case (*t* "domains" in a *c* matrix) is likewise untenable, as a CBED probe incident upon a cubic

matrix with the expected three (3) *t* variants present would produce an "averaged" 2mm <110> zone axis symmetry, and not the m symmetry observed.

While the structure of Y-CSZ has long been accepted as a distorted fluorite structure, the determination of a primitive lattice has additional implications in regards to structure/property relationships. In particular, if the $P\bar{4}3m$ structure determined at room temperature is the stable high temperature phase, the Burgers vector of glissile dislocations would be expected to be <100> rather than <110>; only the latter type has been observed (Dominguez-Rodriguez, Heuer and Castaing 1991). However, if a primitive → face centered cubic structural transformation (analogous to the temperature-dependent order/disorder transformation proposed for Ca-CSZ and Y-CSZ (Carter and Roth 1968, Faber *et al.* 1978, Morinaga *et al.* 1979)) does occur, this might explain the unusually high brittle-to-ductile-transition temperatures of these materials. This idea is worthy of further attention.

Conclusions

A new cubic structure (space group $P\bar{4}3m$), has been determined by CBED analysis for 9.9 and 18 mol% YSZ; the oxygen sublattice is distorted from the ideal fluorite structure by displacements along the <111> directions. Computer-simulated 2-D ZOLZ CBED patterns confirm the experimentally-determined space group and suggest oxygen displacements of ~0.3Å.

ACKNOWLEDGMENTS

We acknowledge useful discussions with J. A. Eades. and support from Los Alamos National Laboratory

References

Buxton, B. F., Eades, J. A., Steeds, J. W. and Rackman, G. M., (1976). *Phil. Trans. R. Soc.* **281**, 171-194.

Carter, R. E., and Roth, W. L., (1968). Electromotive Force Measurements in High-Temperature Systems edited by C. B. Alcock, pp. 125-144. London: Institution of Mining and Metallurgy.

Catlow, C. R. A., Chadwick, A. V., Greaves, G. N. and Moroney, L. M., (1986). *J. Am. Ceram. Soc.* **69**, 272-277.

Dominguez-Rodriguez, A., Heuer, A. H. and Castaing, J., (1991). *Radiation Effects and Defects in Solids* **119-121**, 759-69.

Faber Jr., J., Mueller, M. H. and Cooper, B. R., (1978). *Phys. Rev. B* **17**, 4884-4888.

Horiuchi, H., Schultz, A. J., Leung, P. C., and Williams, J. M., (1984). *Acta Cryst.* **B40**, 367-372.

Howard, C. J., Hill, R. J., and Reichert, B. E., (1988). *Acta Cryst.* **B44**, 116-120.

Howard, C. J. and Hill, R. J., (1991). *J. Mater. Sci.* **26**, 127-134.

McCullough, J. D., and Trueblood, K. N., (1959). *Acta Cryst.* **12**, 507- 511.

Morinaga, M., Adachi, H. and Tsukada, M., (1983). *J. Phys. Chem. Solids* **44**, 301-306.

Morinaga, M., Cohen J. B., and Faber Jr., J., (1979). *Acta Cryst.* **A35**, 789-795.

Morinaga, M., Cohen J. B., and Faber Jr., J., (1980). *Acta Cryst.* **A36**, 520-30.

Osborn, R., Andersen, N. H., Clausen, K., Hackett, M. A., Hayes, W., Hutchings, M. T. and MacDonald, J. E. (1986). *Materials Science Forum* **7**, 55-62.

Randle, V., Barker, I. and Ralph, B., (1989). *J. Electron Microsc.* **13**, 51-65.

Scott, H. G., (1975). *J. Mater. Sci.* **10**, 1527-1535.

Stadelmann, P. A., (1987).*Ultramicroscopy* **21**, 131-146.

Steele, D., and Fender, B. E. F., (1974). *J. Phys. C: Solid State Phys.* **7**, 1-11.

Stubican, V. S. and Hellmann, J. R., (1981). Advances in Ceramics, Vol. 3, edited by A. H. Heuer and L. W. Hobbs, pp. 25-36. Columbus: American Ceramic Society.

Tanaka, M., (1989). *J. Electron Microsc.* **13**, 27-39.

Tanaka, M., Saito, R. and Sekii, H., (1983). *Acta Cryst.* **A39**, 357-368.

Tanaka, M., Sekii, H. and Nagasawa, T., (1983). *Acta Cryst.* **A39**, 825-837.

Teufer, G., (1962). *Acta Cryst.* **15**, 1187.

Zhou, Y., Lei, T.-C. and Sakuma, T., (1991). *Am. Ceram. Soc.* **74**, 633-640.

Appendix

The following table summarizes the various studies relating to anion displacements in stabilized ZrO_2's. Discrepancies exist between the results, but the variety of sample forms and preparation techniques make comparison difficult. All previous work has attempted to determine distortions from an assumed fluorite structure, but have not considered the implications of the displacements from $Fm\bar{3}m$ symmetry.

Authors	Stabilizer	Technique	Sample Form	Direction of Anion Displacement
Carter & Roth (1968)	CaO	neutron diffraction	Polycrystal	<111>
Steele & Fender (1974)	Y_2O_3	neutron diffraction	Polycrystal	<100>, some <111>
Faber Jr., Mueller & Cooper (1978)	CaO & Y_2O_3	neutron diffraction	Single Crystal	<100>
Morinaga, Cohen & Faber Jr. (1979)	CaO & Y_2O_3	x-ray diffraction	Single Crystal	<100>
Horiuchi, Schultz, Leung & Williams (1984)	Y_2O_3	TOF neutron diffraction	Single Crystal	<111>, some <100> at high temperatures
Catlow, Chadwick, Greaves & Moroney (1986)	Y_2O_3	EXAFS	Polycrystal	<100> and <111>
Howard, Hill & Reichert (1988)	MgO	neutron diffraction	Polycrystal	<111>
Howard & Hill (1991)	Y_2O_3	neutron diffraction	Polycrystal	<111>
present study	Y_2O_3	CBED	Single Crystal	<111>

TABLE 1

EXPERIMENTALLY OBSERVED SYMMETRIES

	<111>		<100>		<110>	
	BF	WP	BF	WP	BF*	WP
3.2 mol% (t-ZrO_2)	m	m	2mm	2mm	--	2mm
9.9 mol%	3m	3m	4mm	2mm	--	m
18 mol% (c-ZrO_2)	3m	3m	4mm	4mm	--	2mm

* BF symmetry is not defined for Kossel pattern conditions

TABLE 2

SYMMETRIES PREDICTED FOR t-ZrO_2 AND THE FIVE CUBIC POINT GROUPS

	<111>		<100>		<110>	
	BF	WP	BF	WP	BF	WP
<u>t-ZrO_2</u>					2	2
4/mmm	m	m	2mm	2mm	mm	mm
<u>c-ZrO_2</u>						
$m\bar{3}m$	3m	3m	4mm	4mm	2mm	2mm
$\bar{4}3m$	3m	3m	4mm	2mm	2mm	m
432	3m	3	4mm	4	2mm	2
$m\bar{3}$	3	3	2m m	2mm	m	m
23	3	3	2mm	2	m	1

TABLE 3

PROPOSED ATOMIC POSITIONS FOR A QUADRUPLY PRIMITIVE UNIT CELL OF Y-CSZ FOR THE $P\bar{4}3m$ SPACE GROUP

Atom Type	Wyckoff Position	Atomic Coordinates			
1-Zr	1(a)	0,0,0			
3-Zr	3(c)	0,1/2,1/2	1/2,0,1/2	1/2,1/2,0	
4-O	4(e)	x,x,x	$\bar{x},\bar{x},x$	$\bar{x},x,\bar{x}$	$x,\bar{x},\bar{x}$
4-O	4(e)	x',x',x'	$\bar{x}',\bar{x}',x'$	$\bar{x}',x',\bar{x}'$	$x',\bar{x}',\bar{x}'$

where $x=\frac{1}{4}-\delta$ and $x'=\frac{3}{4}-\gamma$

Figure 1: 9.9 mol% Y-CSZ selected area diffraction patterns of a) <111>, b) <110> and c) <100> zone axes. As expected for this solute composition, the patterns suggest fcc symmetry for this alloy, although {odd, odd, even} type reflections, which are forbidden for the fluorite structure, are visible in the <111> and <110> zone axis patterns.

Figure 2: <111> ZOLZ patterns for the a) 3.2, b) 9.9 mol%, and c) and d) 18 mol% Y-CSZ alloys.

Figure 3: <100> ZOLZ patterns for the a) 3.2 and b) 9.9 mol% alloys.

Figure 4: <110> ZOLZ patterns for the 9.9 mol% YSZ alloys showing a Kossel pattern, a), such that the 000 disc exhibits m WP symmetry (see text for discussion). The 9.9 mol% Kossel-Möllenstadt (K-M) pattern, b), exhibits the BF 2mm and WP m symmetries of the $\bar{4}3m$ point group.

Figure 5: 2-D ZOLZ simulated Kossel pattern, a), for the <110> zone axis. Reduction of the convergence angle yielded a simulated <110> K-M pattern, b), with the WP m and BF 2mm predicted by Buxton, *et al.* (Table 2).

Figure 6: 18 mol% <110> ZOLZ pattern illustrating the subtle m symmetry. The reduction from 2mm symmetry is readily apparent in the (002) and $(2\bar{2}0)$ discs.

Figure 7: Schematic diagrams showing the newly determined cubic structure. The arrows in a) indicate the sense of oxygen displacement, δ, along the cube diagonals. The cations have been removed from this cell for clarity. The [100] projection of the proposed $P\bar{4}3m$ structure, b), illustrates the that the oxygen sublattice consists of two independent sets of 4 oxygens. One set is shifted towards the unit cell corners, while the second is shifted towards the cell center. The magnitude of δ is exaggerated for illustrative purposes.

Figure 8: 2-D ZOLZ simulated patterns (Kossel pattern conditions) for a) <111>, b) <100> and c) <110> zone axes using a foil thickness of 40nm. Oxygen displacements, δ, of 0.3Å along the cube diagonals retain the <100> 4mm symmetry but, gave a <110> m symmetry.

Figure 9: [110] projection of the proposed $P\bar{4}3m$ structure, with the anion displacements exaggerated for effect. The symmetry reduction from 2mm to m is clearly seen in the loss of the $\{1\bar{1}0\}$ mirror plane. The two variants of this structure are related by a 180° rotation about <110>.

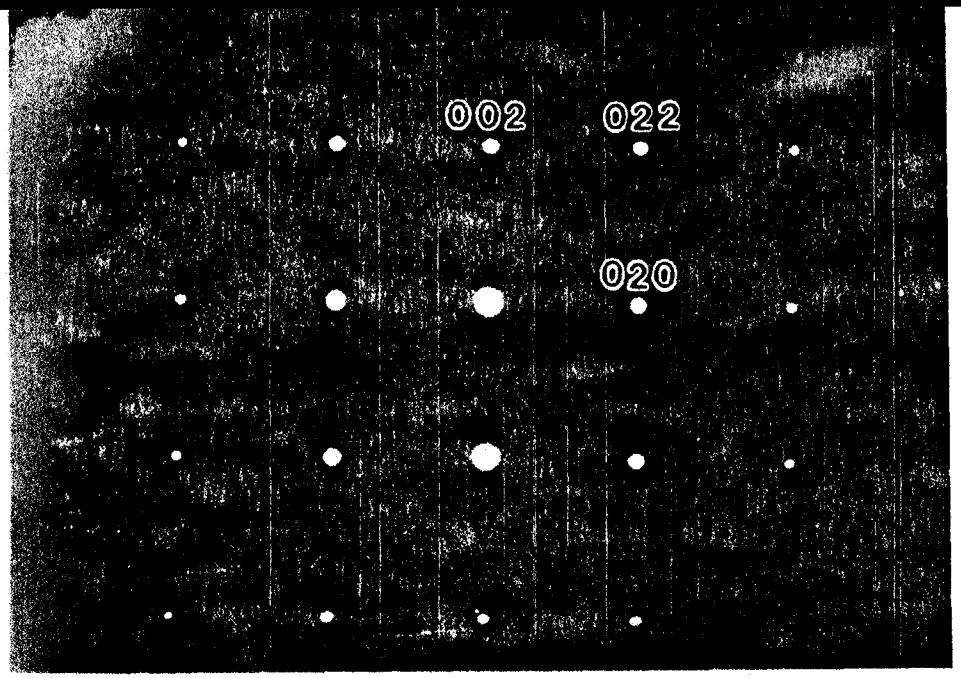
002
022
020

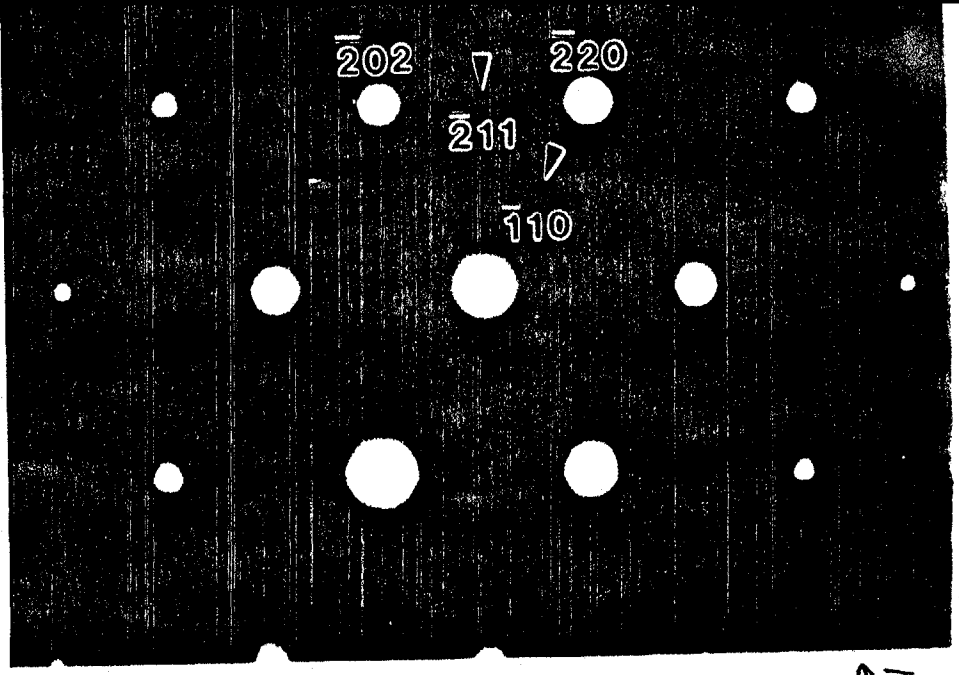
$\bar{2}02$
$\bar{2}20$
$\bar{2}11$
$\bar{1}10$

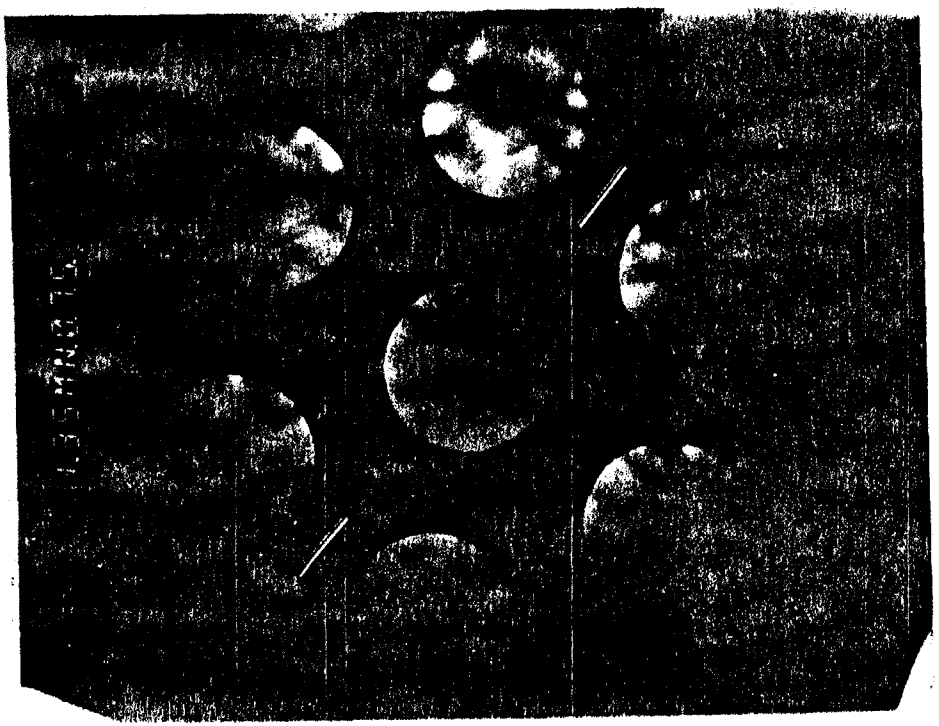

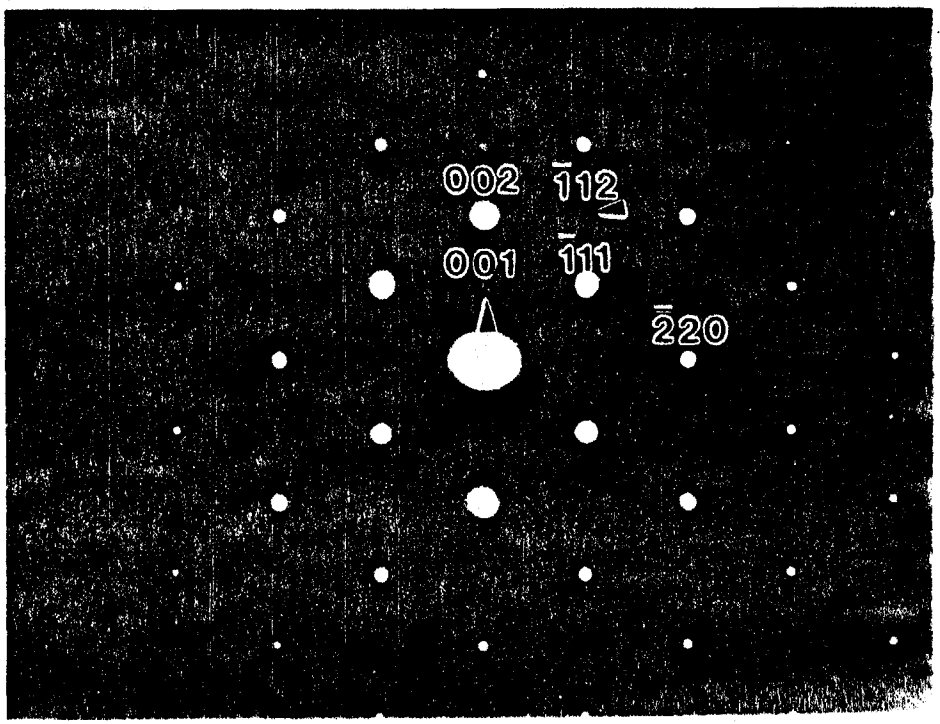
002
$\bar{1}12$
001
$\bar{1}11$
$\bar{2}20$

2b

2c

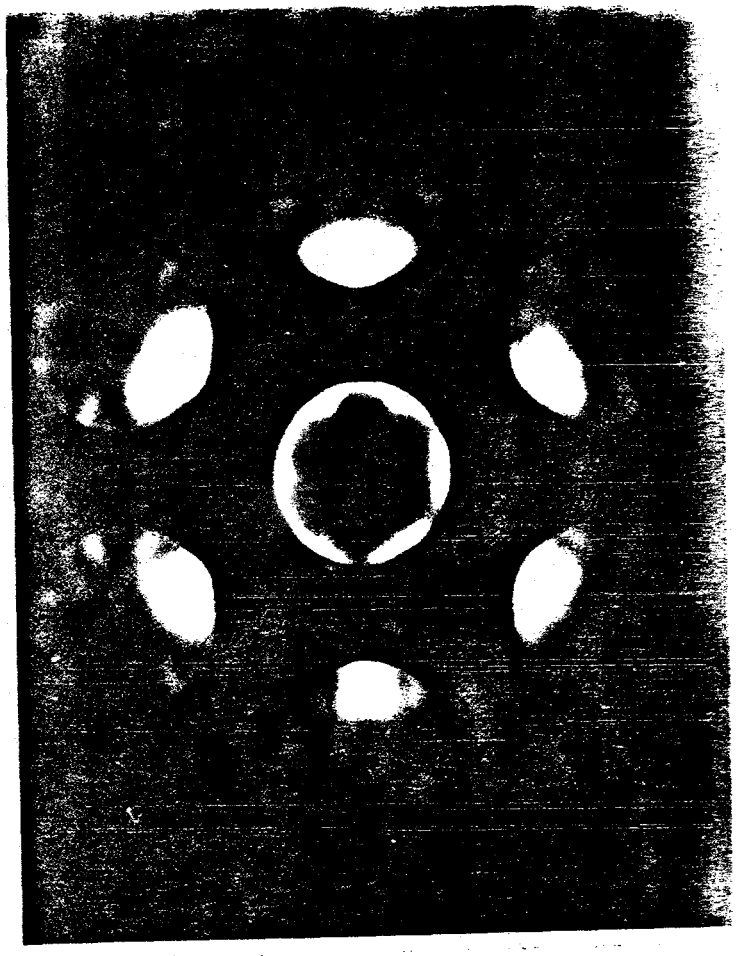

2d

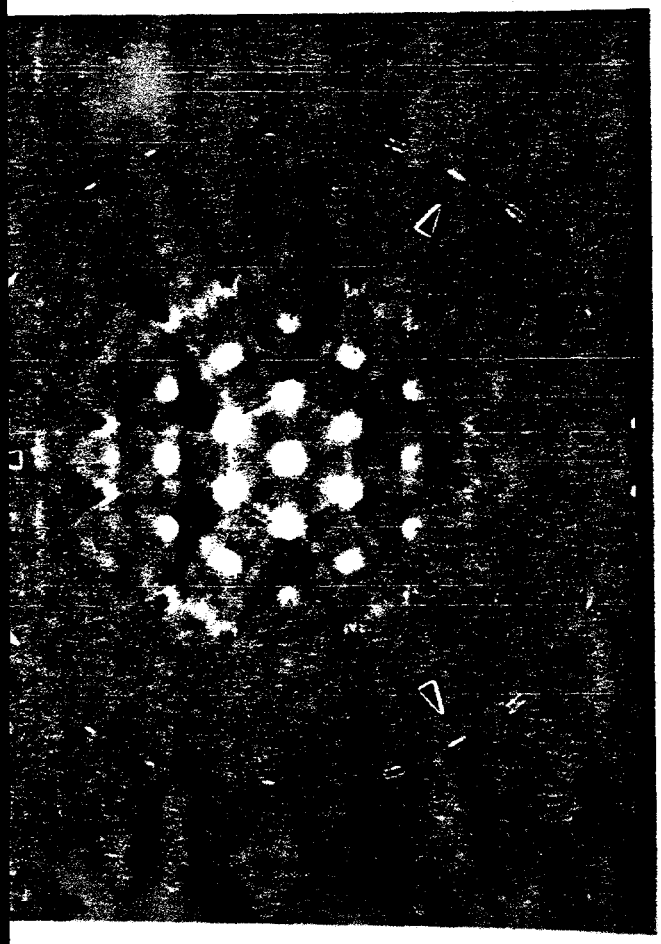

3c

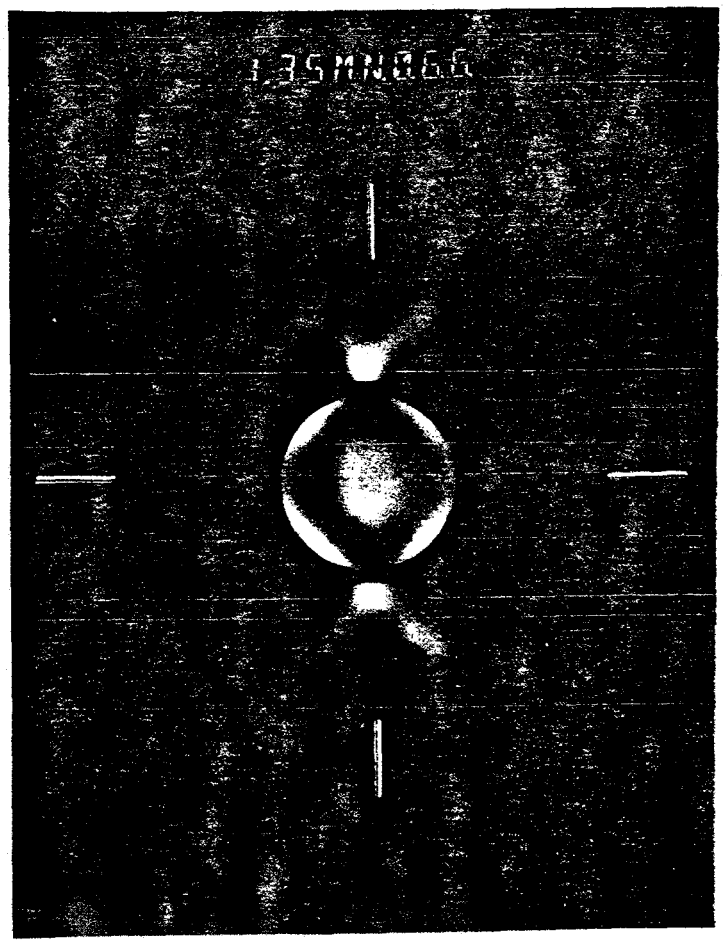

35

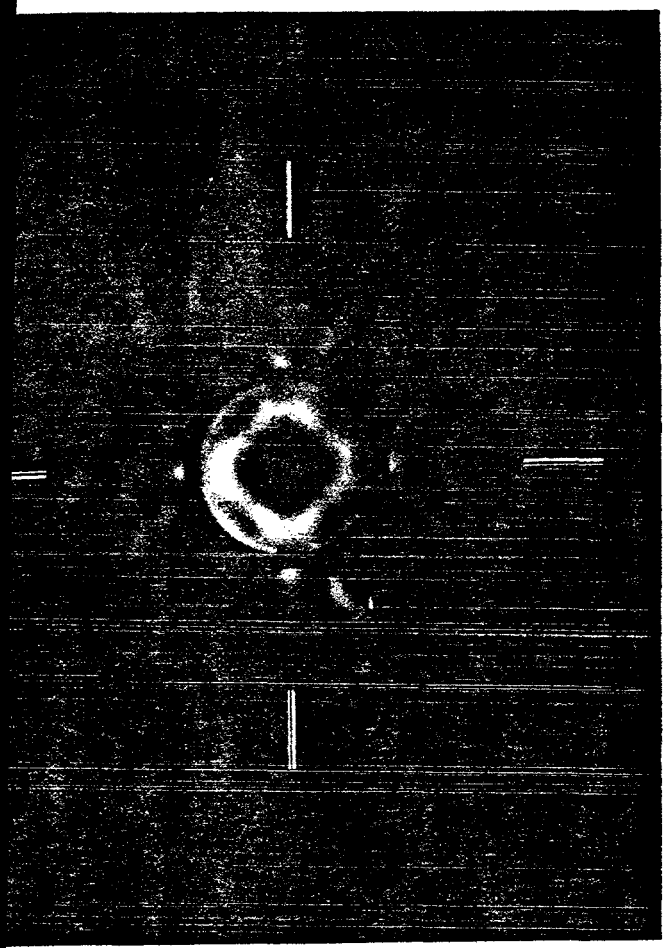

4a

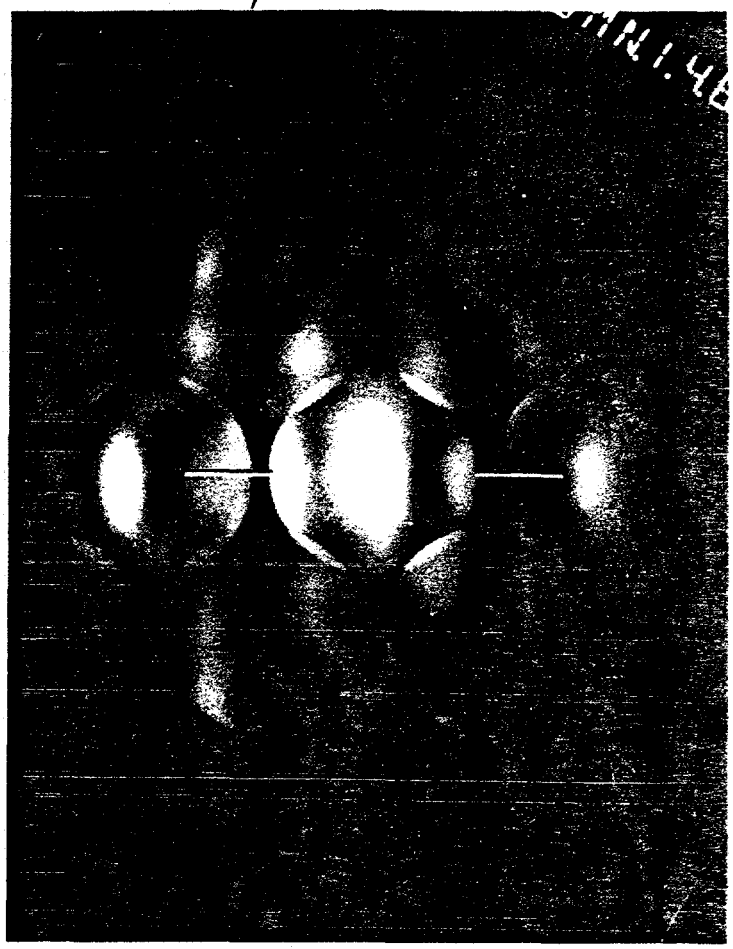

4b

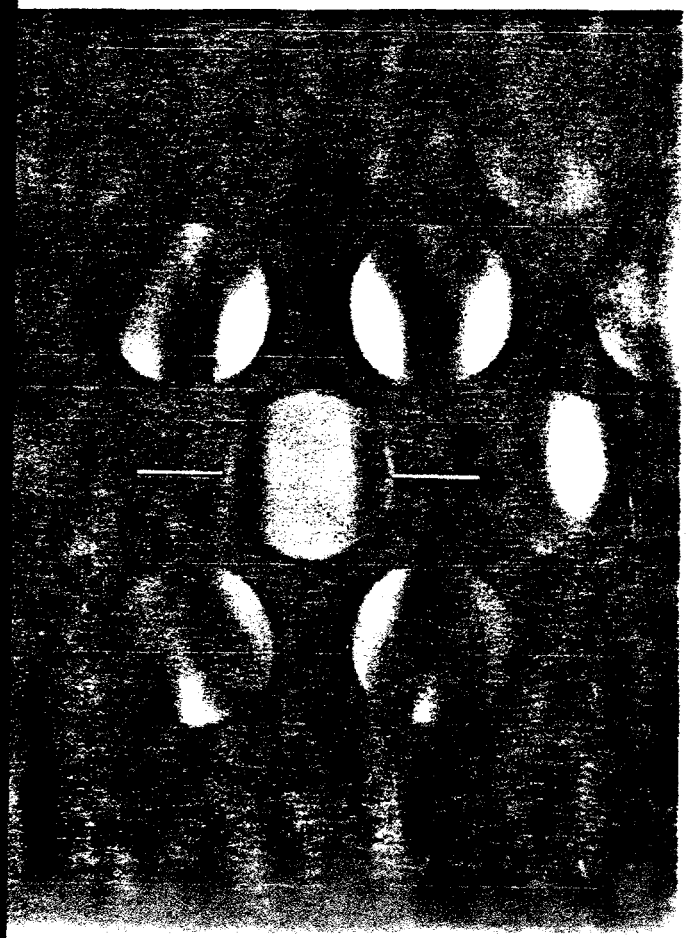

5a

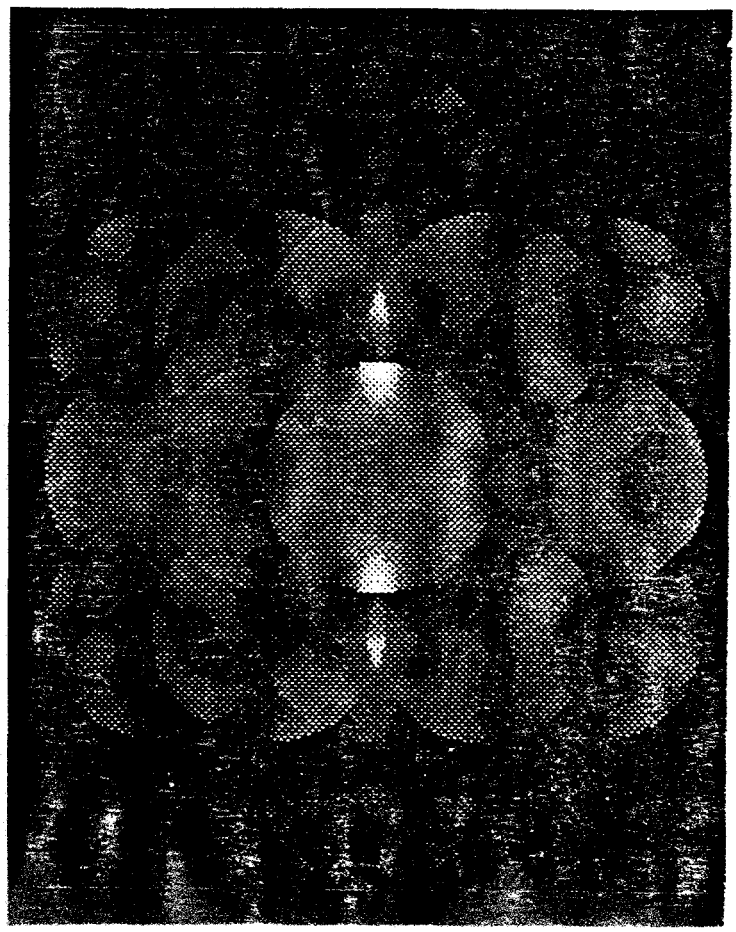

5b

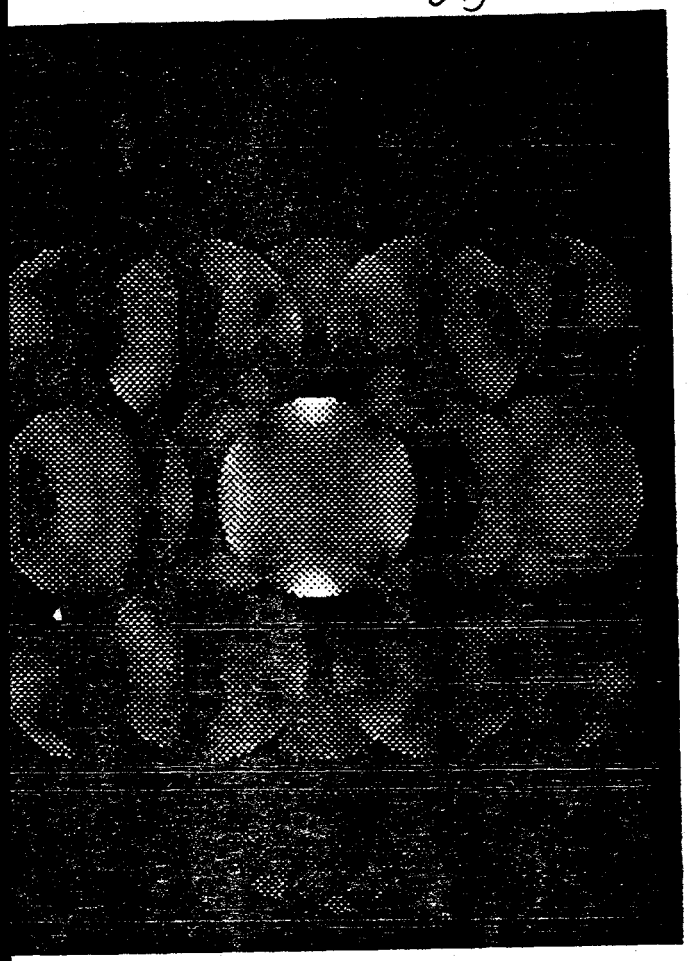

6

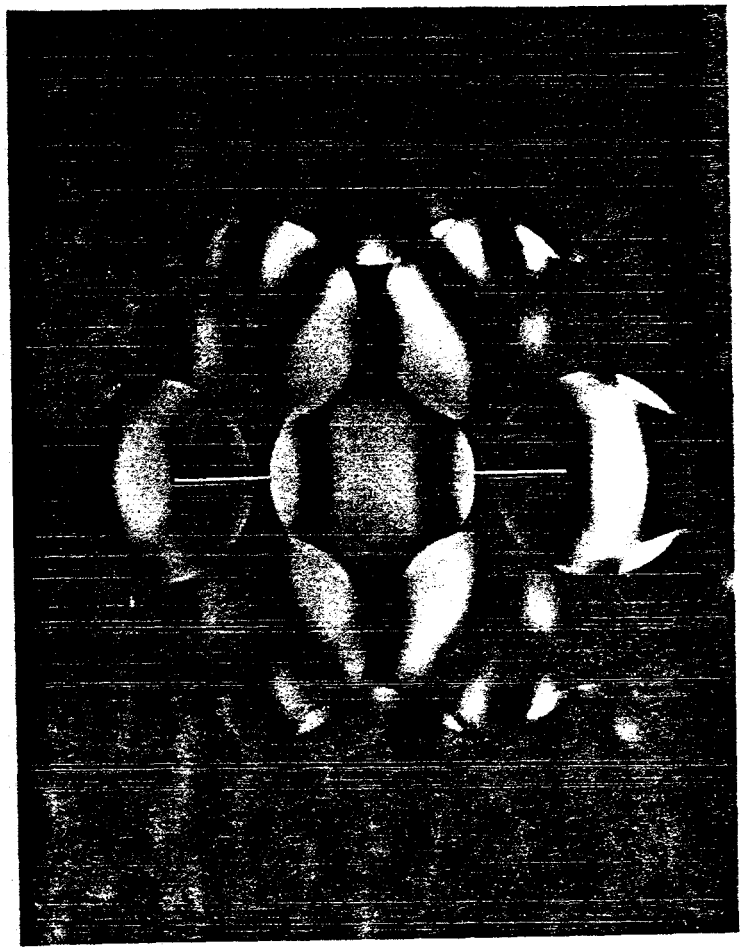

7a.

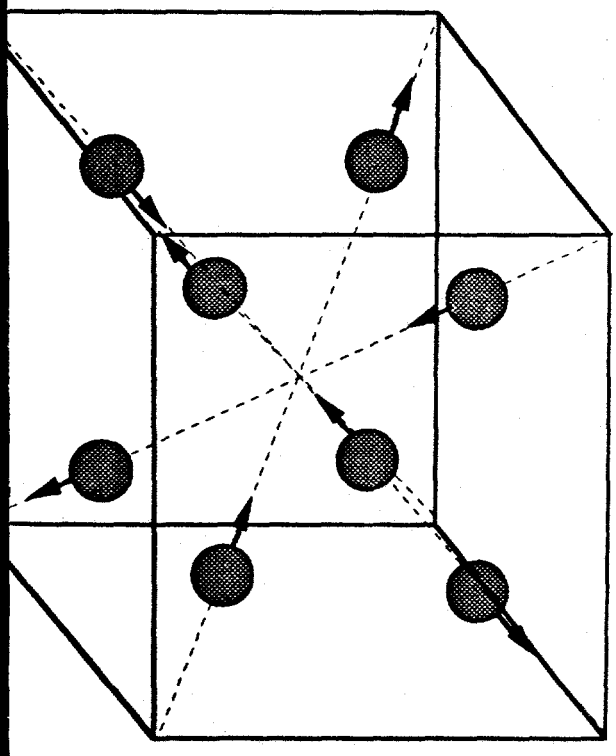

7b

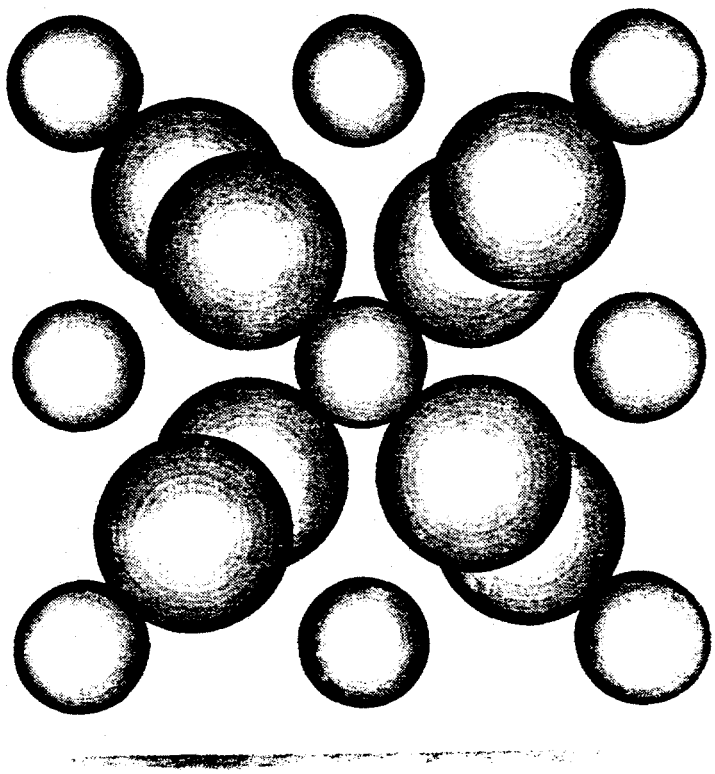

8a

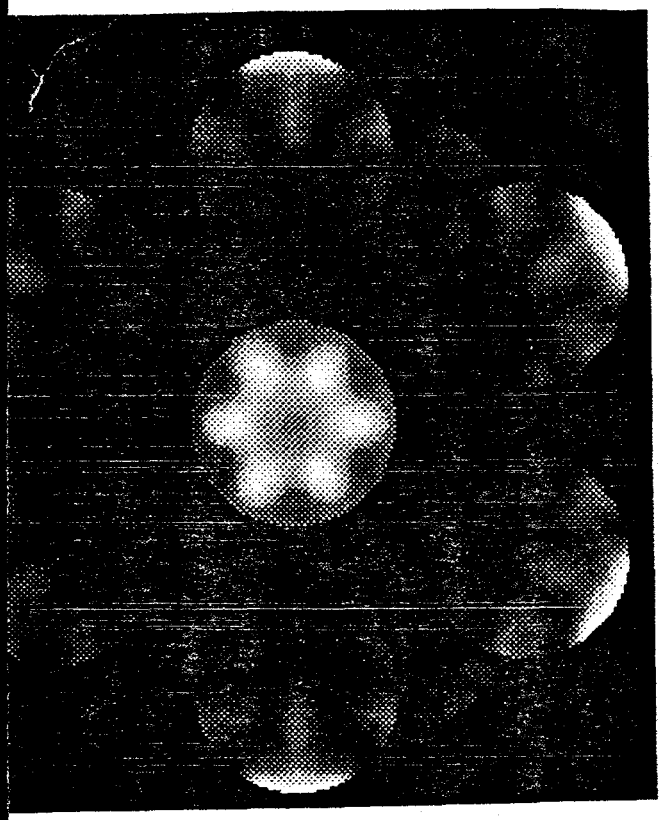

8b

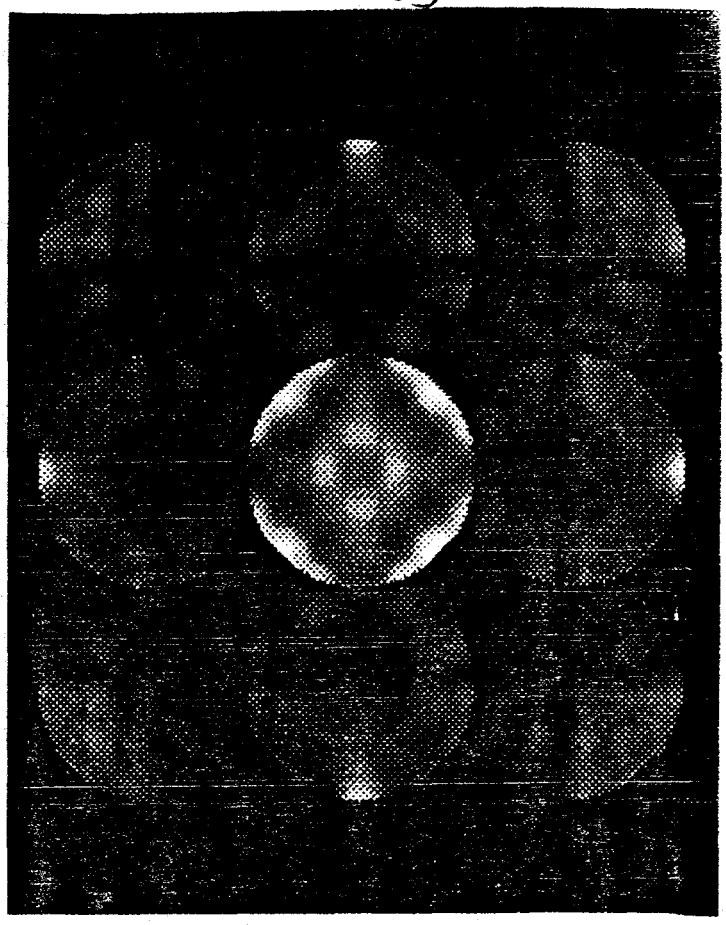

8c

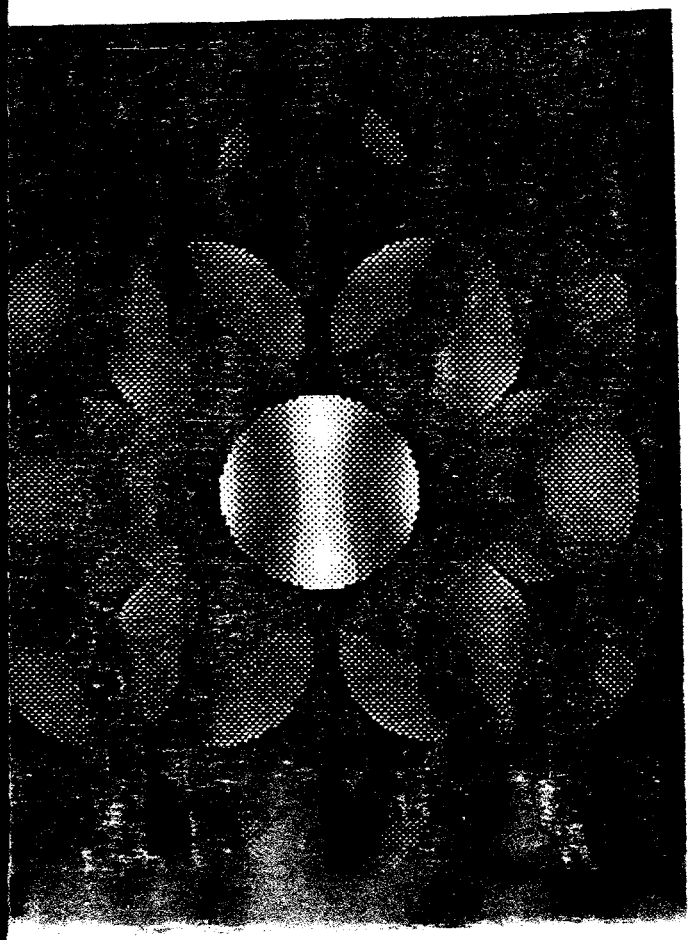

9